Space Weather

RESEARCH ARTICLE

10.1029/2020SW002497

On the Regional Variability of dB/dt and Its Significance to GIC

A. P. Dimmock[1], L. Rosenqvist[2], D. T. Welling[3], A. Viljanen[4], I. Honkonen[4], R. J. Boynton[5], and E. Yordanova[1]

[1]Swedish Institute of Space Physics, Uppsala, Sweden, [2]Swedish Research Defence Agency, Stockholm, Sweden, [3]Department of Physics, University of Texas at Arlington, Arlington, TX, USA, [4]Finnish Meteorological Institute, Helsinki, Finland, [5]Department of Automatic Control and Systems Engineering, University of Sheffield, Sheffield, UK

Key Points:

- The dB/dt measured by individual stations over a region of 500 km can differ by up to a factor of 3
- Regional variability is heavily coupled to solar wind B_z and speed
- Magnetic field spatial variations have an impact on modeling GICs

Correspondence to:
A. P. Dimmock,
andrew.dimmock@irfu.se

Citation:
Dimmock, A. P., Rosenqvist, L., Welling, D. T., Viljanen, A., Honkonen, I., Boynton, R. J., & Yordanova, E. (2020). On the regional variability of dB/dt and its significance to GIC. *Space Weather*, *18*, e2020SW002497. https://doi.org/10.1029/2020SW002497

Received 12 MAR 2020
Accepted 23 JUN 2020
Accepted article online 25 JUN 2020

Abstract Faraday's law of induction is responsible for setting up a geoelectric field due to the variations in the geomagnetic field caused by ionospheric currents. This drives geomagnetically induced currents (GICs) which flow in large ground-based technological infrastructure such as high-voltage power lines. The geoelectric field is often a localized phenomenon exhibiting significant variations over spatial scales of only hundreds of kilometers. This is due to the complex spatiotemporal behavior of electrical currents flowing in the ionosphere and/or large gradients in the ground conductivity due to highly structured local geological properties. Over some regions, and during large storms, both of these effects become significant. In this study, we quantify the regional variability of dB/dt using closely placed IMAGE stations in northern Fennoscandia. The dependency between regional variability, solar wind conditions, and geomagnetic indices are also investigated. Finally, we assess the significance of spatial geomagnetic variations to modeling GICs across a transmission line. Key results from this study are as follows: (1) Regional geomagnetic disturbances are important in modeling GIC during strong storms; (2) dB/dt can vary by several times up to a factor of three compared to the spatial average; (3) dB/dt and its regional variation is coupled to the energy deposited into the magnetosphere; and (4) regional variability can be more accurately captured and predicted from a local index as opposed to a global one. These results demonstrate the need for denser magnetometer networks at high latitudes where transmission lines extending hundreds of kilometers are present.

Plain Language Summary Society is becoming increasingly dependent on technology vulnerable to space weather, meaning that space weather can affect various aspects of our society. The present paper is concerned with geomagnetically induced currents (GICs), which are created by rapid changes in the Earth's geomagnetic field. They flow in long conducting ground infrastructures such as pipelines, power lines, and railways, resulting in negative effects. Predicting GICs is particularly difficult because their underlying driver, the geoelectric field, can change significantly over geographic areas of only several hundred kilometers, which can be considered highly localized. This work aims to understand this regional variability, its dependency on the solar wind, and the effects this has on GICs. The main results from this work are that the rate of change of the geomagnetic field (1) can vary by factors of 3 over 500 km regions, (2) depends on the amount of energy deposited into the Earth's near-space environment, and (3) can result in GICs which differ by up to 60%. Our results indicate that the local geology is also important to the derivative of the geomagnetic field. These results help to quantify the error in predicting GICs, train new machine-learning algorithms, and understand the physical mechanisms responsible for this behavior.

1. Introduction

Society is becoming increasingly dependent on space and ground-based technological systems, which are vulnerable to space weather. Space weather is a scientific and engineering problem and aims to understand and mitigate the socioeconomic impacts which arise due to the interaction between the solar wind and our magnetosphere. This is a significant challenge; in some cases, the chain of events originates under the solar surface and extends deep below ground. Geomagnetically induced currents (GICs) are a prime example of an end-link of the full space weather chain. They affect long conducting ground networks such as power lines, telecommunication cables, railways, and pipelines.

Spatiotemporal variations in electrical currents flowing in the magnetosphere and ionosphere cause rapid variations of the geomagnetic field ($\mathrm{d}B/\mathrm{d}t$) measured on the surface. Due to the conductive nature of the ground and Faraday's law of induction, an accompanying geoelectric field will be set up, causing currents to flow in long conducting systems (Pulkkinen, 2015). Depending on the frequency of the geomagnetic field variations, the relevant ground conductivity structures to be considered can extend hundreds of kilometers below the surface depending on the skin depth. Thus, geoelectric fields and GICs are also sensitive to geological properties and highly conductive seawater. GICs have been reported to inflict physical damage on hardware (Anderson et al., 1974; Bolduc, 2002; Boteler & Jansen Van Beek, 1999; Pulkkinen et al., 2005; Rosenqvist et al., 2005), motivating new governmental policy (see Pulkkinen et al., 2017) and risk assessments (e.g., Eastwood et al., 2017) to arise.

Although GICs have been studied for many decades (Anderson et al., 1974; Kappenman, 2003; Lehtinen & Pirjola, 1985; Pulkkinen et al., 2015; Viljanen, 1997), there are many unresolved questions in the physical processes which drive them. In particular, it has been known for some time that GICs can be a localized phenomenon (Anderson et al., 1974), and this remains a challenge in GIC research to date. This challenge pertains to the incomplete physical understanding of the magnetosphere-ionosphere coupling processes driving local geomagnetic features, and also the inability for global near-space plasma simulations to resolve some of these smaller-scale phenomena. In general, regional variability is caused by the complex dynamical behavior of small-scale ionospheric currents (Pulkkinen et al., 2003) and/or complex ground conductivity features (Bedrosian & Love, 2015; Kelbert, 2020). The former requires a solid understanding of the numerous solar wind-magnetosphere-ionosphere coupling processes such as substorms (Akasofu, 1964; Kan et al., 1991). The latter depends on the accurate high-resolution magnetotelluric (MT) surveying of ground conductivity features over a given region to build realistic conductivity maps. Each of these tasks is crucial since, in reality, regional variations of the geoelectric field is always the complex combination of these two factors. Overcoming these problems has been a major focus of previous studies and continues to be the case today.

Using subsets of the IMAGE magnetometer network, Pulkkinen et al. (2015) analyzed spatial averages of the geoelectric field spanning a region of ∼500 km. In certain conditions, station-specific values of the geoelectric field were 5 times larger than the regional average. This demonstrates that the spatial structure of the geoelectric field can be highly complex, and individual stations can produce vastly different values compared to neighboring ones. Although recordings at a single point can be successfully used as a regional proxy for GIC (Viljanen et al., 2015), to realistically model GIC at single power grid substations, an accurate description of the geoelectric field as a function of time and space is needed, and the assumption of a spatially uniform field may no longer be applicable (Kelbert, 2020).

Ngwira et al. (2015) have shown that during intense geomagnetic storms, the geoelectric field can manifest as extreme localized peak enhancements. It was suggested that the source mechanism could be localized substorm events (Tsurutani et al., 2015). More recently, Ngwira et al. (2018) studied localized $\mathrm{d}B/\mathrm{d}t$ variations during two geomagnetic storms. The authors report that intense $\mathrm{d}B/\mathrm{d}t$ followed the poleward edge of the poleward moving aurora. This corresponds to the region of strongest aurora during a substorm and supports their previous results. This does not close the matter however since Ngwira et al. (2018) states that further work is needed to clarify the exact magnetosphere-ionosphere coupling processes responsible. Nevertheless, this is consistent with Viljanen, Tanskanen, et al. (2006), who reported that the occurrence of the largest GICs concentrates around local midnight when substorms are a typical ionospheric phenomenon. Another peak time of large $\mathrm{d}B/\mathrm{d}t$, or large time derivatives of equivalent ionospheric current densities, is the dawn sector (Juusola et al., 2015; Viljanen et al., 2001; Viljanen, Tanskanen, et al. 2006; Weigel et al., 2003). In addition to these, auroral omega bands are another phenomenon which can be responsible for large $\mathrm{d}B/\mathrm{d}t$ and GIC events (Apatenkov et al., 2020).

The formation of the substorm current wedge will form a strong westward electrojet current around midnight Magnetic Local Time (MLT) (see Milan et al., 2017), which generally occurs multiple times per day. However, Viljanen, Tanskanen, et al. (2006) showed that substorms that occur during geomagnetic storms tend to produce higher levels of $\mathrm{d}B/\mathrm{d}t$. Recent evidence by Freeman et al. (2019) suggests that the DP2 current is the dominant source of $\mathrm{d}H/\mathrm{d}t > 600$ nT/min, which they state could be damaging to the UK National Grid. Other studies have reported observational evidence that rapid changes in eastward currents outside of the midnight sector can also drive large GICs (Boteler & Jansen Van Beek, 1999; Dimmock et al., 2019). Thus, more work is needed to understand these complex current systems, how they couple to the magnetosphere, and their potential impact on ground-based systems.

It is not only the magnitude of the geoelectric field which is important, but the orientation of the vector with respect to a network also plays a critical role in GICs. Viljanen and Pirjola (2017) investigated the outcome when the geoelectric field has a fixed average magnitude (1 V/km) in a studied power grid but spatially varying vector patterns over regional (10–100 km) scales. They report that when the vector geoelectric field is spatially nonuniform, the sum (from all substations) of GICs exhibit a wider range. Thus, Viljanen and Pirjola (2017) explicitly show that nonuniform fields can lead to larger-amplitude GICs. Of course, there are cases when orientations of nonuniform fields may produce smaller GICs than uniform fields, but the key point is that the geometry between local geoelectric fields and the transmission lines are important, and it is required to accurately determine the geoelectric field vector pattern even over regional scales. Identifying the key magnetosphere-ionosphere processes driving such behavior will also be crucial. In a study performed by Love et al. (2019), the authors report that in regions where the geoelectric field hazard was greatest, the geoelectric field tended to be more polarized. The opposite was true for the least geoelectric hazard. To understand extreme events, we must primarily understand the drivers in the ionosphere and, secondarily, the effect of local ground conductivity.

When modeling the geoelectric field, the ground conductivity plays an important role (Bedrosian & Love, 2015). Bedrosian and Love (2015) investigated the effects on geoelectric fields due to the three-dimensional Earth conductivity over the midwestern United States. They used a synthetic input which was a geographically uniform sinusoidal function representing the geomagnetic field. Therefore, any differences were solely due to the geographically varying conductivity structures. Their 3-D model results for a sinusoidally varying spatially uniform magnetic field produces geoelectric fields with an average amplitude of about 2.71 V/km, but having a notable site-to-site range of 0.15 to 16.77 V/km. Other studies have also shown the importance of 3-D models (Honkonen et al., 2018; Ivannikova et al., 2018; Liu et al., 2018) which include lateral conductivity gradients. However, it should also be mentioned that 1-D models have sometimes performed reasonably well (Viljanen, Pulkkinen, et al. 2006). The use of 1-D models can be justified in regions far from large lateral conductivity gradients such as the coastal effect or inland geological features. Nevertheless, it is apparent that geological features are important, and therefore, determining the most applicable ground conductivity model to a given region is key to performing an accurate GIC hazard assessment (Kelbert, 2020).

To accurately forecast GICs, the ground magnetic field is required, and this can be obtained experimentally, or calculated from numerical models. Ideally, the model would be used since it can provide the ground magnetic field at any location while simultaneously providing the global context and possible origin of geomagnetic disturbances. Therefore, it is important to investigate the performance of models in numerous scenarios. As part of a Space Weather Prediction Center (SWPC) challenge (Pulkkinen et al., 2013), Tóth et al. (2014) assessed the capabilities of the Space Weather Modeling Framework (SWMF) (Tóth et al., 2005) to predict dB/dt. One significant outcome from this work was that it was easier to predict the magnetic perturbation than its derivative. Since the magnetic perturbation magnitude and corresponding derivative were empirically related, then a higher success was achieved by first predicting the perturbation, and then applying the empirical relation to evaluate the derivative. Honkonen et al. (2018) modeled the chain from the magnetosphere to the geoelectric field by coupling a global magnetohydrodynamic (MHD) model to an electrostatic ionosphere and then a 3-D conductivity model. The authors noted that the inability for global MHD models to capture small-scale ionospheric processes is a large source of error which limits the forecasting of the geoelectric field and subsequently, GICs.

From the literature, it is clear that there are open questions pertaining to the impact on GICs from regional variations of dB/dt and the ground conductivity. Also, it remains unclear to what extent can global models produce spatially structured geomagnetic disturbances. The purpose of this study is to address these open questions. First, we quantify the regional variation of dB/dt using ground magnetometer recordings; second, solar wind drivers are identified based on OMNI data; finally, we investigate the impact of varying dB/dt on GICs by comparing the voltages induced across 200 km hypothetical transmission lines when a spatially uniform magnetic field is assumed, and when it is not.

10.1029/2020SW002497

The manuscript is structured as follows. Section 2 provides a technical description of the data and models used to conduct this study. The following section 3 describes the adopted methodologies used to produce our results, which are presented in section 4. The detailed physical description and interpretations of our results are reserved for the discussion in section 5. Finally, we draw our conclusions and provide a summary in section 6.

2. Data and Models

2.1. Solar Wind

For solar wind monitoring, plasma and field parameters from the OMNI database were employed. These data are obtained via the OMNIWeb service (http://omniweb.gsfc.nasa.gov), and the 60-s high-resolution data set was selected. Initially, these measurements are conducted upstream close to the L1 point by multiple spacecraft (e.g., ACE, Wind, DSCOVR), and then later they are propagated (King & Papitashvili, 2005) to the bow shock nose location according to the Farris and Russell (1994) bow shock model. As a result, these parameters were not measured in situ at the bow shock nose, but are representative of conditions at that location.

2.2. Ground Magnetometer Measurements

To analyze the geomagnetic response on the ground, we used measurements collected by the IMAGE (Tanskanen, 2009) magnetometer network. In total, the network is composed of 41 stations spanning a geographic latitude range of 51–79° over the Baltic and Fennoscandian region. A map showing all of the stations is located in Figure 1. Due to the middle to high latitudinal range, this network is well suited for studying the geomagnetic influences felt from the auroral electrojet currents. Each station employs at least 10-s time resolution, ideal for resolving small temporal-scale features and accurately measuring dB/dt. It is well-known that dB/dt is quite sensitive to the temporal resolution, and lower cadence data can significantly underestimate dB/dt (Pulkkinen, Viljanen, et al. 2006). Note that in this study we will express units in nT/min using IMAGE to compare with other studies; however, these quantities are calculated using the 10-s data and not averaged to 1 min. It is also advantageous that the dense coverage notably between latitudes 65 and 70° enables the resolution of regional (100–500 km) spatial scale structures that originate in the ionosphere. Such features are prominent during geomagnetic storms. Their rapid spatiotemporal behavior enhances dB/dt, subsequently causing large GICs.

2.3. Ground Conductivity Models

We employ the crustal conductivity maps established by Korja et al. (2002), which covers the Fennoscandian region including the surrounding seawater (SMAP). Three sheets of fixed thickness are used to devise a full 3-D conductivity model as demonstrated by Figure 2. The conductance in the upper layer (0–10 km) is shown in panel a and includes seawater, sediment, upper crust, and the surface. The well-known coastal effect is produced by this layer in which there is a sharp gradient between the highly conductive seawater and low ground conductivity. The middle (10–30 km) and lower (30–60 km) crusts are shown in panels (b) and (c), respectively. These layers are placed according to panel (d) above the lowest layer, which is the deep crust/mantle and represents depths below 60 km. This conductivity is set at $\sigma_\infty=10^{-3}$ S/m, consistent with the 60–100 km layer in the Engels and Korja (2002) standard normal model. By converting depth to conductance in bathymetric data, the conductivity of the water was estimated in which the Baltic sea salinity variations were accounted for (Rosenqvist & Hall, 2019). The conductivity of the bedrock was determined from 1-D and 3-D MT surveys over the region. For a more thorough description of this model, including validation and implementation, we refer readers to Rosenqvist and Hall (2019).

3. Methods and Data Processing

3.1. Processing of Experimental Data

This study aims to investigate (from a statistical standpoint) the extent of spatial variations of dB/dt over a region of ~500 km, given the current availability of long-term observations. We apply 17 years of solar wind and geomagnetic recordings (January 2000 to December 2017) which require a quantitative and automated routine to measure the regional variability. We adopted a similar approach to Pulkkinen et al. (2015) using the IMAGE network. In their study, spatial averages of the geoelectric field were calculated from several

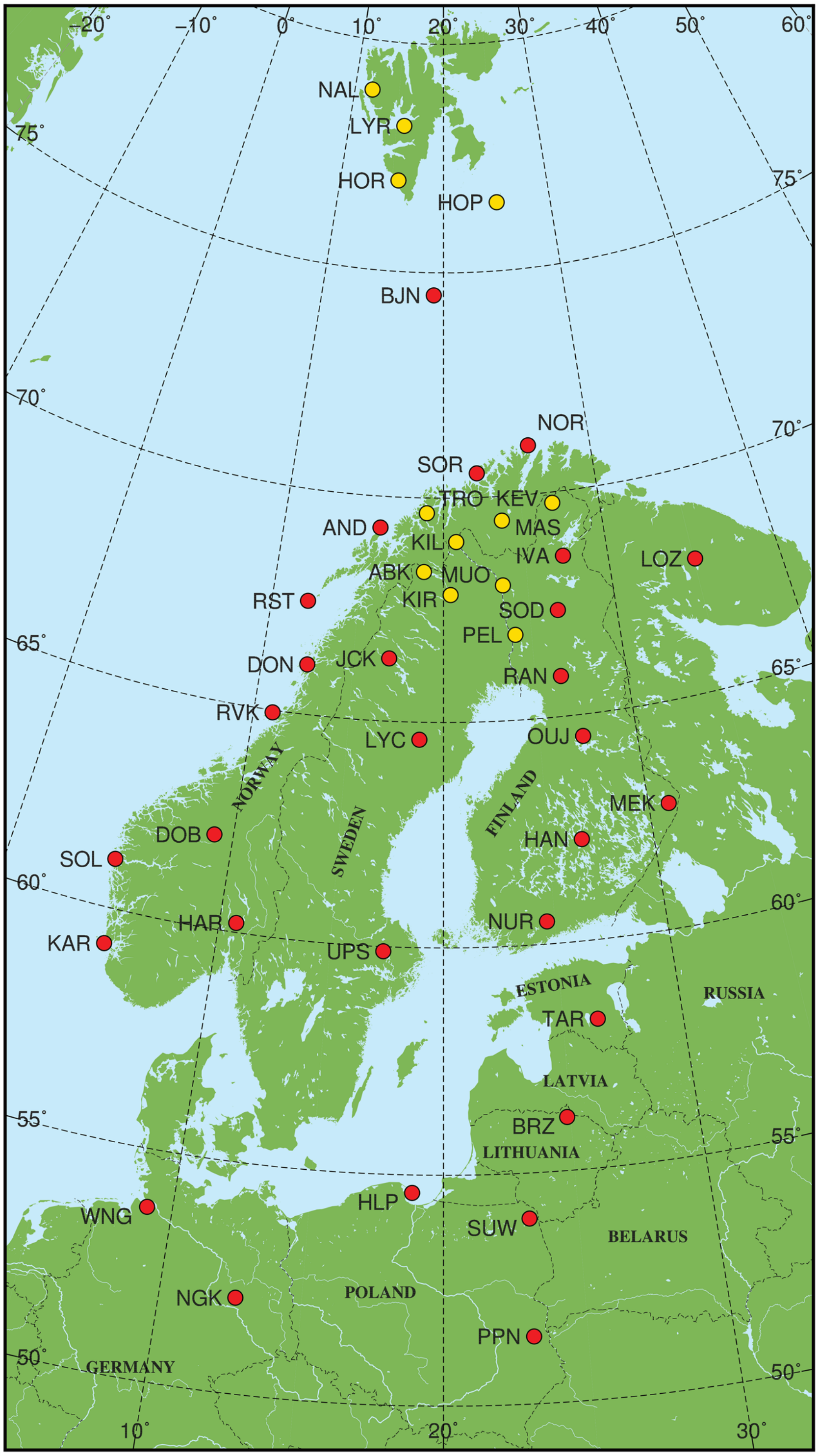

Figure 1. Map of Fennoscandia and the positions of the magnetometer stations comprising the IMAGE network. The yellow dots indicate subsets of stations used in this study to quantify the regional variability of dB/dt. The red dots indicate the locations of the remaining stations. At the time of this study, IMAGE included 41 active stations.

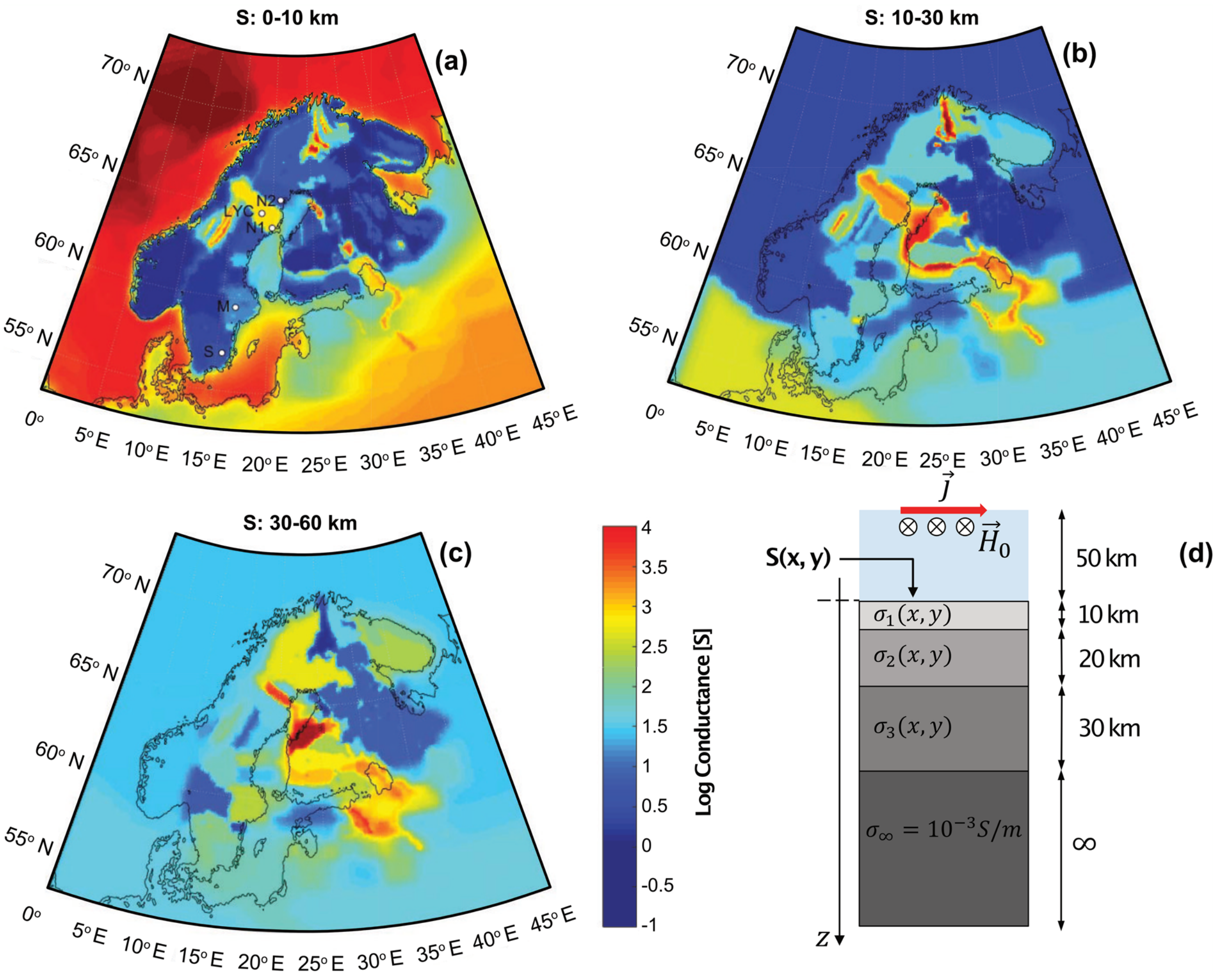

Figure 2. Schematic showing the conductance distributions $S(x,y,z)$ used to create the 3-D conductivity model. The model comprises three layers of fixed depth, of which the distributions of lateral conductance $S(x,y)$ are shown in panels (a)–(c). Panel (a) covers 0–10 km and includes the seawater, sediment, upper crust, and surface. Panel (b) corresponds to the middle crust between 10 and 30 km. Panel (c) represents the lower crust at depths between 30 and 60 km. Panel (d) illustrates the model and the arrangement of each layer. The underlying bedrock (z=60→∞) is added as a final layer, and set to $\sigma_\infty = 10^{-3}$ S/m.

Table 1
The Two Selected Subsets of IMAGE Stations and Corresponding Geographical Coordinates

Subset (S)	Subset station # (i)	Station	Code	GLat (°)	GLon (°)
1	1	Hopen Island	HOP	76.51	25.01
1	2	Hornsund	HOR	77.00	15.60
1	3	Longyearbyen	LYR	78.20	15.82
1	4	Ny Ålesund	NAL	78.92	11.95
2	1	Abisko	ABK	68.35	18.82
2	2	Kevo	KEV	69.76	27.07
2	3	Kilpisjärvi	KIL	69.06	20.77
2	4	Kiruna	KIR	67.84	20.42
2	5	Masi	MAS	69.46	23.07
2	6	Muonio	MUO	68.02	25.53
2	7	Pello	PEL	66.90	24.08
2	8	Tromsø	TRO	69.66	18.94

Note. See yellow markers in Figure 1 for their locations on the Fennoscandia map.

nearby magnetometer stations which could be compared to station-specific values. The implementation of this requires a sufficiently dense network of magnetometers on scales approaching just a few hundred kilometers. A large-scale network consisting of interstation separation on this level is not currently realized, but parts of existing networks such as IMAGE do satisfy this requirement. As demonstrated by Pulkkinen et al. (2015), subsets from IMAGE can effectively provide a local/regional network of stations interseparated by ~100 km over several hundred kilometers. Therefore, we selected two subsets of stations at two narrow latitude ranges where the network was suitably dense. Details of these stations are listed in Table 1. The IMAGE network is shown in Figure 1 and the subsets are highlighted using yellow dots.

The subset time series are used to derive a metric that describes the region-to-specific difference (*RSD*) of dB/dt. In practice, the *RSD* is another time series matching the temporal resolution of the IMAGE data. The *RSD* is essentially a comparison between a single station

$\mathrm{d}H/\mathrm{d}t$ and the average of another set of stations. Here, $\mathrm{d}H/\mathrm{d}t$ corresponds to the magnitude of the horizontal components $\mathrm{d}H/\mathrm{d}t = \sqrt{(\mathrm{d}B_x/\mathrm{d}t)^2 + (\mathrm{d}B_y/\mathrm{d}t)^2}$. In this study, the other stations are a subset of the IMAGE network and the average indicates the regional average. To compute *RSD*, the first step is to compute $RSD_{ss} = \mathrm{d}H/\mathrm{d}t^{ss} - \mathrm{d}H/\mathrm{d}t^{ra}$ for each station, where superscripts *ss* and *ra* correspond to station specific and regional average, respectively. Note that the regional average does not include the station which is currently being considered, and RSD_{ss} can be positive or negative. The second step is to identify $RSD_{max} = max(|RSD_{ss}|)$ at each time step. The value passed to the final *RSD* time series is then the value of RSD_{ss} corresponding to the indices of RSD_{max}, thus the polarity of *RSD* is retained. Positive *RSD* correspond to scenarios when a single station measures a $\mathrm{d}H/\mathrm{d}t$ larger than the regional average, negative *RSD* stems from when the largest regional variation is from one station measuring a very small $\mathrm{d}H/\mathrm{d}t$ compared to the regional average. The motivation in this study is the former, which are the localized peak geoelectric field enhancements reported by Ngwira et al. (2015). For this reason, we only consider positive *RSD* and in the following text *RSD* refers to $RSD > 0$. In fact, $RSD < 0$ is far less common and these points constitute approximately only 7% of the combined RSD data set. It should be said that negative *RSD* also present an interesting situation, but since their underlying driving mechanisms may be different, and this was not the motivation for the present study, we defer any analysis of this to future investigations. In addition, since there are markedly fewer data points for these cases, they are not ideally suited to the level of statistical analysis that was performed in this study.

The *RSD* is available at 10-s cadence; however, this is difficult to accurately compare with upstream solar wind conditions. For this reason, we identify the maximum positive *RSD* within a 30-min window. The maximum *RSD* within the 30-min window is used as a reference time to compute other parameters such as the solar wind conditions and instantaneous geomagnetic indices. The solar wind properties are calculated by an average within a 20-min window with a delay of 10 min introduced to allow some system propagation. In other words, the start and end points of the 20-min solar wind window are 30 and 10 min prior to the max *RSD*, respectively. In reality, the 10-min delay has a negligible effect on the results and no bearing on the conclusions but was introduced to account for some time for the magnetospheric system to respond. We also introduced a 20-min delay and the results were unchanged. The geomagnetic indices are calculated by taking the mean over a 5-min window centered around the peak *RSD*.

4. Results

Figure 3 shows an example of *RSD* for Region 2 for the well-documented space weather events of September 2017. From panel (c), it is clear that in strong events such as this, the regional variability of $\mathrm{d}H/\mathrm{d}t$ is significant and stations often simultaneously measure markedly different values. In many cases, a few stations together have large $|\mathrm{d}H/\mathrm{d}t|$ compared to the remaining ones; however, in some cases just one station has markedly different $|\mathrm{d}H/\mathrm{d}t|$ to all the others (e.g. around 01:40). The majority of these regional variations are likely associated with substorms and a sudden storm commencement which has been documented by Dimmock et al. (2019). They also occur during southward IMF and solar wind speeds above 400 km/s. It is this regional variability and solar wind dependency that we will analyze from a statistical standpoint in the remaining manuscript. This variability will also be studied in the context of the impact on GIC modeling.

4.1. Statistical Analysis of IMAGE Data

In Figure 4, the relationship between the *RSD* and the regional average is shown in the form of scatter plots. The top row (a and b) corresponds to subset one, whereas the bottom row (c and d) is subset two. The left and right columns show the same data set, except they are plotted on linear and logarithmic scales, respectively. The dashed red trace in panels (a) and (d) indicate when the *RSD* would be equal to the regional average. For both subsets, the general trend is that as the regional average increases, so does the *RSD* magnitude and spread. This dependency is more clearly seen on a log scale, and in general, the possible *RSD* range for any given regional average can be large, sometimes by an order of magnitude. We should mention that for display purposes, several data points are located outside the limits of these axes, but this range was selected to better highlight the statistical dependency. Interestingly, the vast majority of data points are

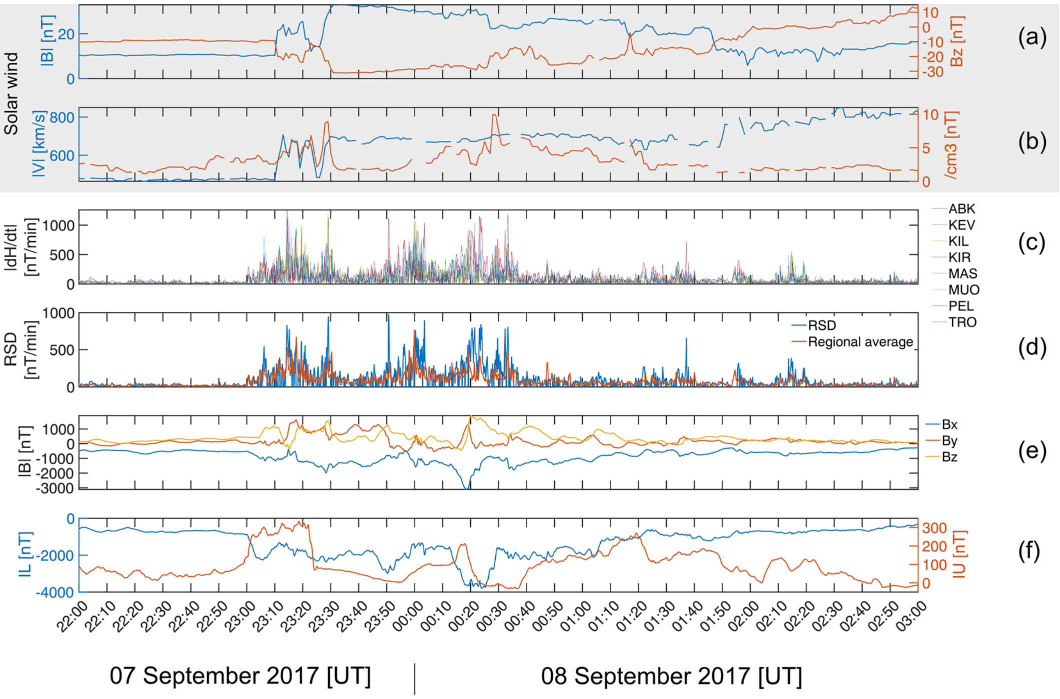

Figure 3. Example of *RSD* for the September 2017 event. Panels (a) and (b) are solar wind parameters from OMNI. Panels (c) and (d) are the |d*H*/d*t*| and |*RSD*| for the Region 2 stations. Note that *RSD* used here is at 10-s resolution, but the following statistical analysis uses the 30 min maximum. The recordings at the Kiruna magnetometer are included for reference. The IMAGE derived IL and IU indices are displayed in the bottom panel.

located above the red line, suggesting that the *RSD* typically exceeds the regional average. In other words, over this region, one station typically sees a significantly larger d*H*/d*t* compared to the others. In fact, in many cases, the *RSD* is several times the regional average, indicating a surprisingly high degree of spatial variation and structure. What can be concluded here is that when there is activity in the form of a large regional d*H*/d*t*, the spatial variation will likely be on a similar order of magnitude to this value. What is also interesting is the difference between the two subsets. In fact, subset two appears to obey a more ordered dependency. For example, when the regional average is around 300 nT/min, the range of *RSD* is narrower in panel (d) compared to that in panel (b). That is to say, the tip of the data cluster is much narrower in panel (d) compared to that in panel (b). It should also be noted that the range of *RSD* for low to middle (10–100 nT/min) regional averages is noticeably larger for subset one compared to subset two.

A comparison between the *RSD* and auroral geomagnetic indices is made in Figure 5. Here, the global AE index is shown together with its equivalent computed from the IMAGE stations (IE). The difference between these two is that the IE has latitudinal coverage and is restricted to the Fennoscandian MLT sector, and is thus a local index concerning the stations we have used (Kauristie et al., 1996). Similar to Figure 4, the top and bottom rows correspond to the different subsets, but on the other hand, the left and right columns represent the IE and AE indices, respectively. Although an expected relationship with the *RSD* is evident, there are some interesting features to mention. First, again there seems to be a difference between the subsets in the sense that subset two shows a sharper dependency. This is more obvious in the IE index when comparing panels (a) and (c). Another interesting feature to point out is the lower range of *RSD* in panel (c). Although the upper range of *RSD* increases steadily with IE, the lower range sharply increases when IE exceeds 200 nT. As a result, the range thereafter narrows, but this is not observed in panel (a). As a consequence, for strong auroral activity (IE ∼ 1,000 nT), the range of *RSD* in subset one remains extensive but appears significantly narrower in panel (c). A similar effect manifests when comparing the results for IE and AE for subset two in panels (c) and (d). Therefore, the local index and subset two demonstrate a better correlation with *RSD*. Nevertheless, the observation that larger IE gives rise to larger possible *RSD* is evident in both subsets and is also applicable to the AL index.

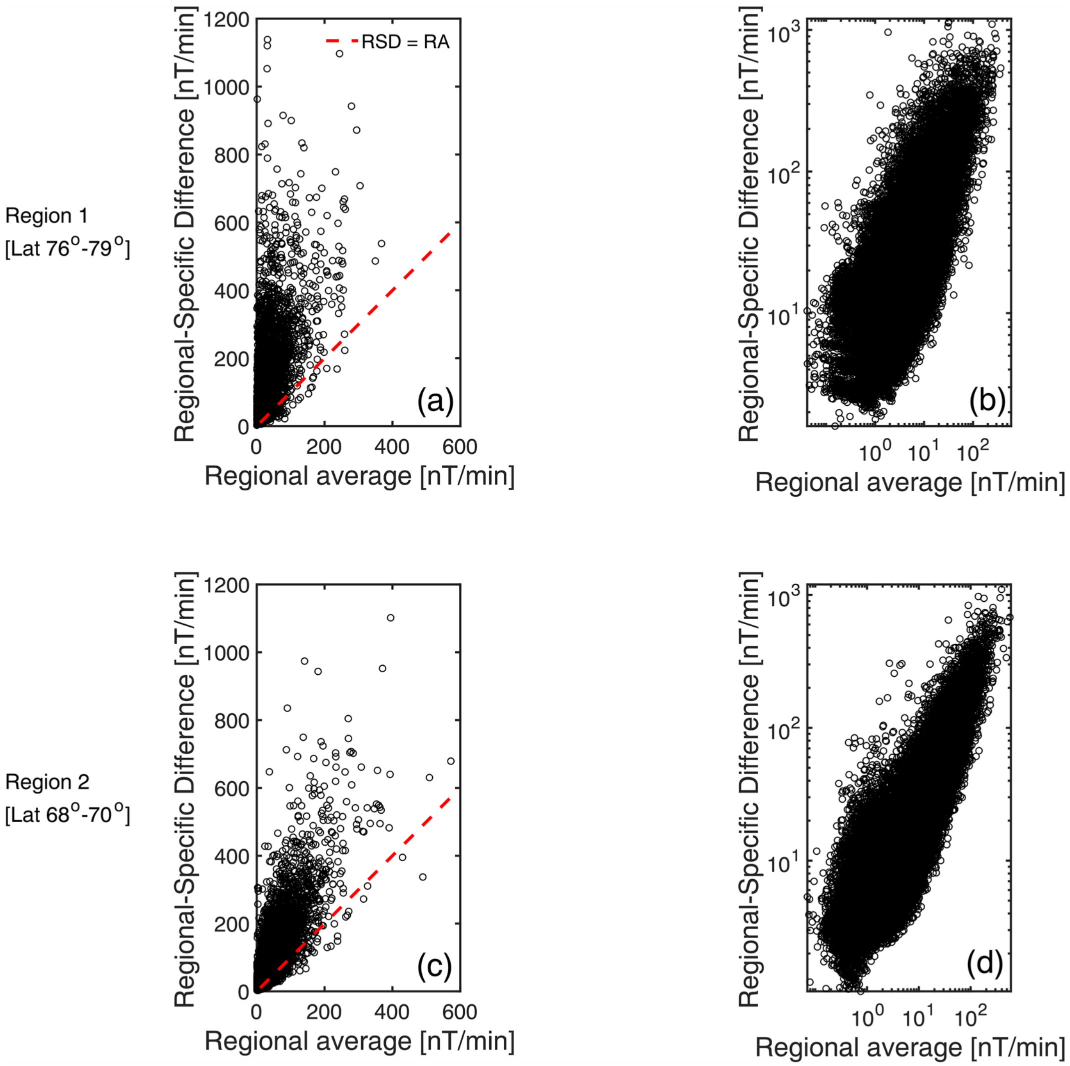

Figure 4. The *RSD* as a function of regional average for subsets one (a and b) and two (c and d). The left and right columns correspond to linear and logarithmic scales, respectively. The dashed red line in the left column indicates when the *RSD* would be the same as the regional average. The tendency for increased regional variation with the regional average is apparent in all panels.

The relation between the *RSD* and the IMF B_z component is investigated in Figure 6 for subset two. The plot is organized such that the *RSD* is plotted on the *x* axis and B_z on the *y* axis. The *RSD* has been split into three ranges corresponding to orders of magnitude: 1–10 (a1), 10–100 (b1), and 100–1,000 (c1). Panels (a2), (b2), and (c2) show the percentage of points which are northward (>0) and southward (<0) within each range. The red dashed line marks B_z=0. It becomes immediately obvious that larger *RSD* (>100 nT/min) are generally associated with southward IMF. In fact, according to panel (c2), around 85% of the points are southward in panel (c1). Although the midrange of *RSD* is composed of both northward and southward IMF, the aforementioned trend is evident when the *RSD* approaches 50 nT/min. In general, during intervals of little to no regional variability (*RSD*<10 nT/min), the IMF is predominantly northward. Nevertheless, even for *RSD*<10 nT/min, there are around 40% of the points which are southward, and even 15% of the points are northward in panel (c1). This suggests a multiparameter dependency beyond simply considering the southward component of the IMF.

In Figure 7, the solar wind-*RSD* dependency is studied in more detail. Panels (a)–(c) show the probability density functions (PDFs) of the *RSD* and additional subsets according to geomagnetic indices and

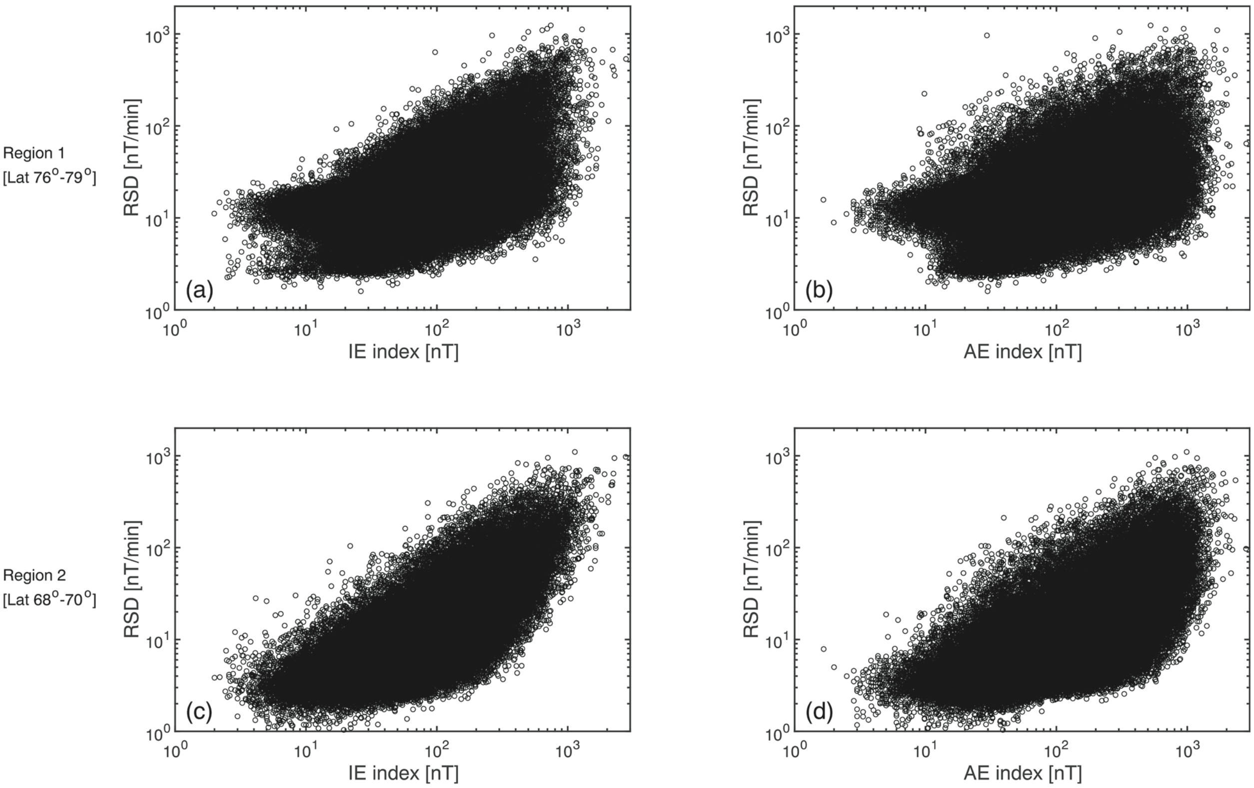

Figure 5. The *RSD* as a function of IE (a and c) and AE (b and d) geomagnetic indices for subsets one (a and b) and two (c and d). During stronger IE and AE, there appears to be larger regional variation; however, the statistical relationship is clearer for the local IE index.

upstream conditions. The black PDF is the baseline for all data, whereas the colored traces are the PDFs corresponding to the subsets. Panel (d) shows the 3-D distribution of *RSD*, for B_z and solar wind speed (|*V*|). The bin dimensions were selected so that B_z and |*V*| have an equal number of bins over the parameter space, which equates to widths of 20 km/s and 2 nT for |*V*| and B_z, respectively. It is important to mention that the counts within each bin vary significantly over the parameter range, especially for large values of B_z and |*V*|. We have added a plot showing the bin densities to the appendix (Figure A1) to help the

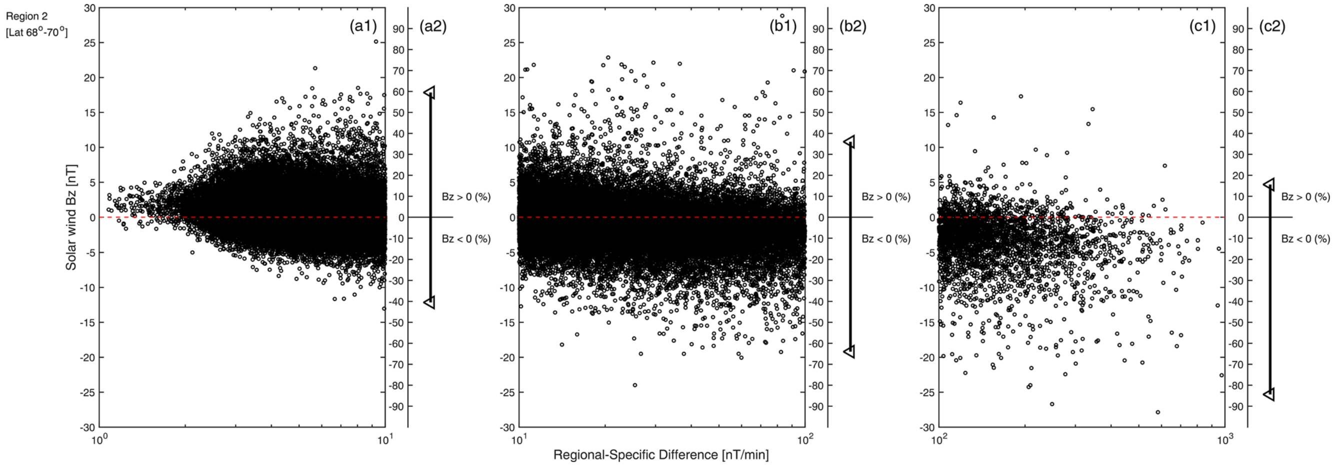

Figure 6. The IMF B_z component plotted against the *RSD* for ranges in orders of magnitude (a1, b1, and c1). Panels (a2), (b2), and (c2) indicate the percentage of points in each range which are northward (>0) and southward (<0). There is a general trend that an increase in spatial d*H*/d*t* variability is expected during southward IMF.

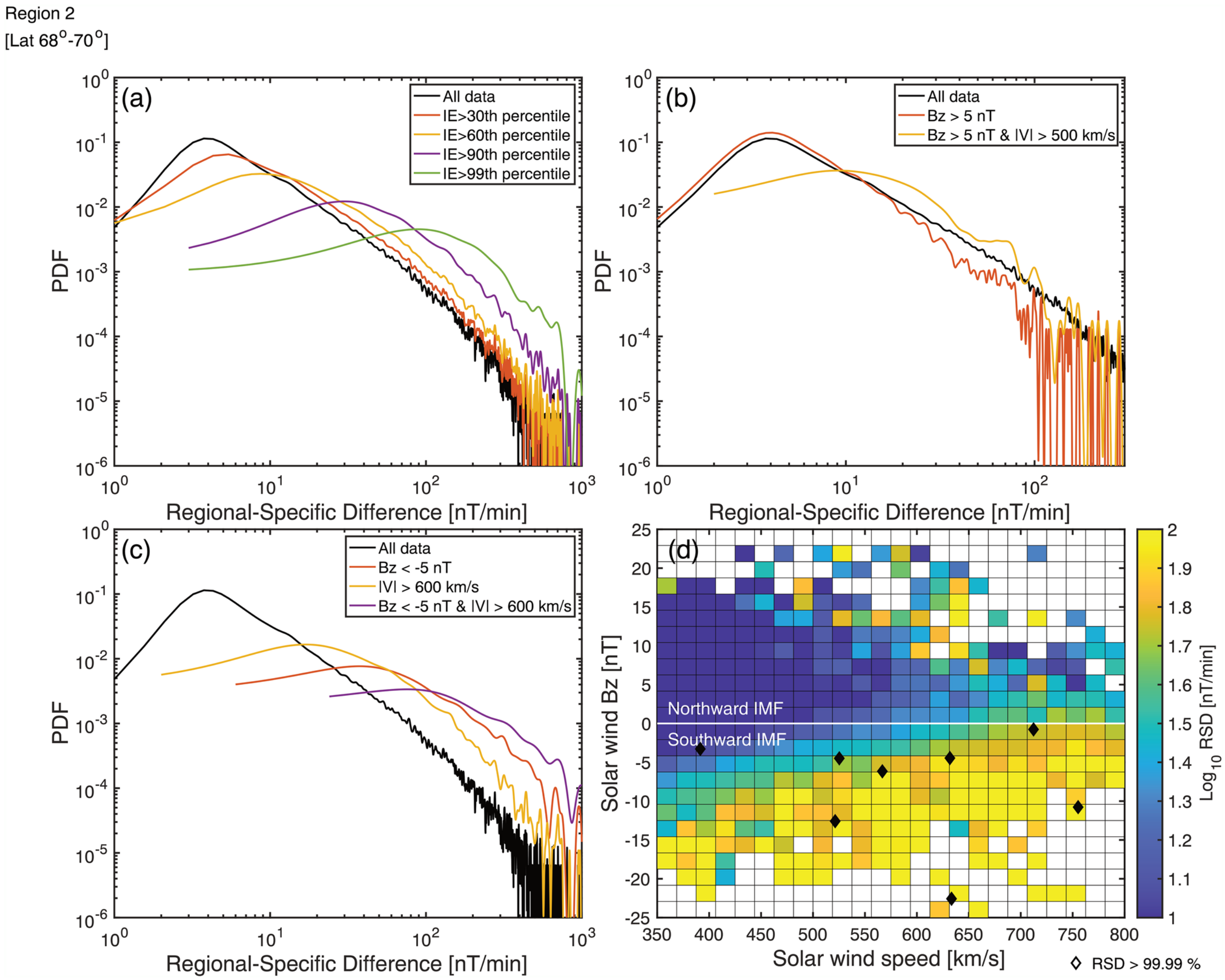

Figure 7. Panels (a)–(c) show the probabilistic dependencies between *RSD* and various upstream solar wind criteria in the form of probability density functions. Panel (d) is a 3-D distribution of *RSD*, B_z, and |*V*|. The color of each bin is an average of *RSD*. In all panels, it is clear that the largest *RSD* favors southward IMF and fast solar wind speed. Note that large *RSD* can also occur during northward IMF, but it is statistically rarer. The diamond markers in panel (d) indicate the B_z and |*V*| locations of the most extreme (>99.99%) *RSD*.

interpretation of Figure 7. The diamond markers indicate the B_z and |*V*| locations of the most extreme (>99.99%) *RSD* values. The two largest events of *RSD* originate from 15 March 2012 and 7 September 2017, which were large geomagnetic storms. The other large events are spread over other intervals corresponding likely to intense substorms. Thus, the extreme (>99.99%) events in this data set do not originate from only one or two single large storms but are distributed across several individual events. For the PDFs in panels (a)–(c), subsets of *RSD* are extracted for a given criterion, and then a PDF is generated based on a kernel density estimation. The PDFs are plotted on a log scale to highlight the effect on the tails of the distributions. The data located in the tails can be considered as the most hazardous conditions.

Similarly to Figure 5, Figure 7a demonstrates that the IE index is correlated to the *RSD*. The largest impact is on the 90th and 99th percentiles, which correspond to IE values of 296 and 711, respectively. Of which, there are 8,334 (833) data points for the 90th (99th) percentile subsets. The purple and green PDFs exhibit more weighted tails compared to the other subsets. For example, the probability of *RSD*>100 nT/min for the 90th and 99th percentile subsets are 25% and 71%, respectively. This is compared to only 5% and 8% for the 30th and 60th percentile subsets, respectively; highlighting that the effect is notably more substantial for the upper quantiles (>90%). Thus, the geomagnetic indices appear only relevant during strong activity.

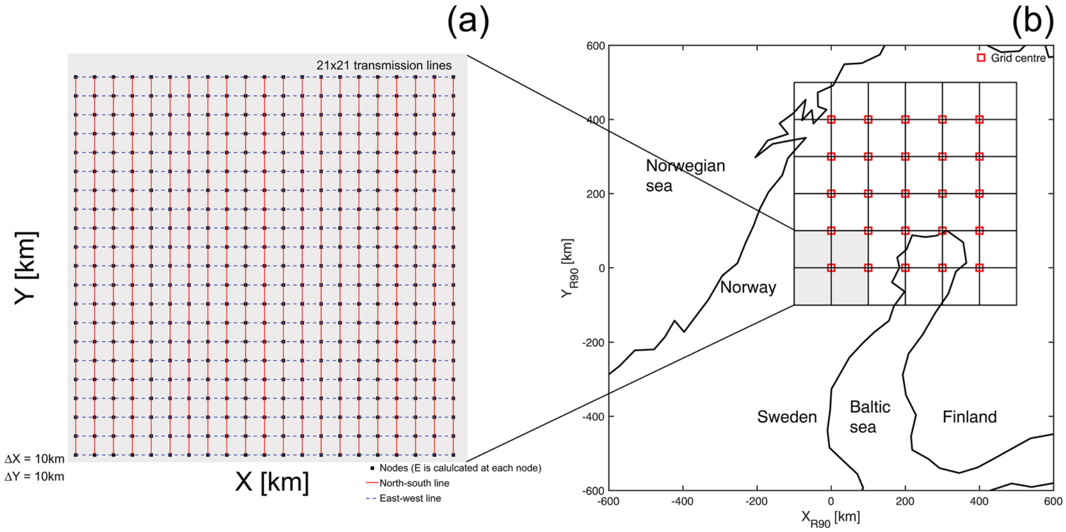

Figure 8. Sketch of the grid layout (a) showing the nodes and lines used to form the hypothetical transmission lines. Panel (b) shows the locations of the grid placements. The red squares indicate the center points of each grid. This region was selected due to the high density of IMAGE stations as shown in Figure 1. Note that repeated lines are excluded and only unique lines are retained.

Shown in Figure 7b is the effect of northward IMF combined with $|V|$ on the RSD. Note that in panel (d), large $RSDs$ start to appear when $|V|>500$ km/s and $B_z>5$ nT, and therefore we have used these values as thresholds to extract the subsets used to compile the PDFs. As demonstrated by the orange line, during northward IMF, the probability of $RSD>100$ nT/min is negligible (~1%). Adding the requirement that $|V|>500$ km/s increases the probability of RSD in the moderate range of 20–100 nT/min, and the effect on $RSD>100$ nT/min suggests a slight increase to around 3%. Therefore, we can say that $RSD \sim 100$ nT/min is possible (but unlikely) during northward IMF, and there is a small increase in likelihood when the solar wind speed is faster.

Figure 7c is similar to the previous panels except that PDFs of RSD for southward IMF, $|V|$, and the combination of both are shown. Similar to before, we have selected subset thresholds where large RSD are prominent during southward IMF, which is when $|V|>600$ km/s and $B_z<-5$ nT. Note that the threshold for large RSD is not necessarily consistent between northward and southward IMF due to the different physical driving. It is immediately obvious that the impact on RSD for these conditions is much more substantial compared to those shown in panel (b). In these cases, the probabilities of $RSD>100$ nT/min for $B_z<-5$ nT, $|V|>600$ km/s, and $B_z<-5$ nT and $|V|>600$ km/s are 38%, 16%, and 62%, respectively. Therefore, the combined criterion of southward IMF and faster speed produce the largest probability of higher RSD.

The results from panels (a)–(c) are summarized in panel (d), in which the RSD is simultaneously binned for B_z and $|V|$ for the parameter space of $-25<B_z<25$ nT and $350<|V|<800$ km/s. There are several interesting features to point out: (1) The RSD is larger for southward IMF and faster speed, as demonstrated in panel (c); (2) northward IMF yields generally low RSD except instances when $V>500$; and (3) the interesting distribution of the RSD during $-B_z$ is indicative of a dependency on solar wind Ey. The diamond markers show the conditions for very extreme $RSD>99.99\%$ data points. All but one of these cases is southward during relatively fast solar wind (>500 km/s). The remaining point occurs for slower speeds and weaker southward IMF conditions, and similar points were present in Figure 6. The outliers are important since it demonstrates that large $\mathrm{d}H/\mathrm{d}t$ and subsequent regional variability does not necessarily occur during the traditionally geoeffective upstream conditions.

4.2. The Impact on GIC

The results so far have provided a clear demonstration that $\mathrm{d}H/\mathrm{d}t$ experiences significant variation over a relatively small region (~500 km). Now we investigate the potential impact that these complex and spatially structured geomagnetic responses may pose to GICs, especially our ability to accurately model them. In

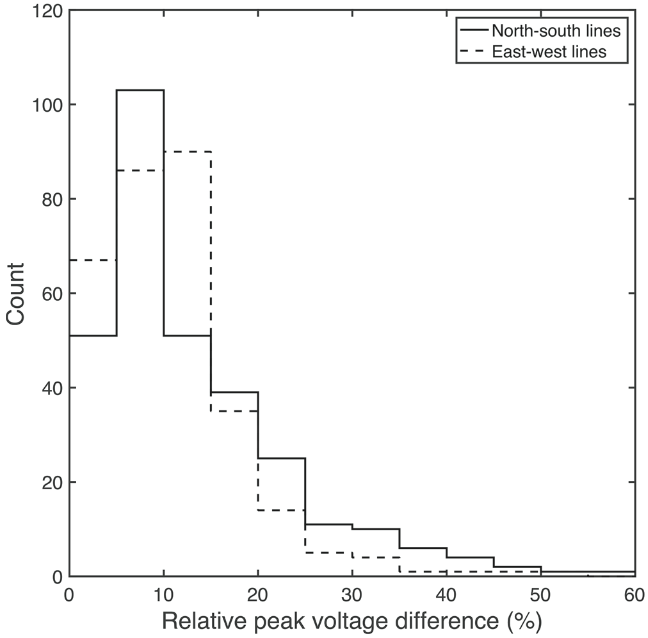

Figure 9. Histogram of relative percentage differences for the peak absolute voltage across north-south (solid black), and east-west (dashed black) transmission lines. The relative percent difference is calculated between two voltages for cases when the same magnetic field is assumed across a line, and a different magnetic field is used for each node shown in Figure 8a.

practice, we adopt a new methodology to assess the effects over a straight-line hypothetical transmission line of fixed length. Initially, we compose a square grid of 200×200 km which is internally composed of nodes separated by 10 km. Figure 8a shows a diagram of this grid configuration. Note that in the context of this study, nodes refer to the points in which we calculate the geoelectric field. Therefore within the square grid, each 200 km transmission line is independent. This differs from real power grids where nodes may refer to the points where longer transmission lines are interconnected.

At each node, the geoelectric field is calculated over the interval 17:15–19:15 on 8 September 2017. Note that IMAGE data are not used directly for this since stations are not available at the exact node locations. To overcome this, the IMAGE network is first used to derive the equivalent currents over the Fennoscandian region based on spherical elementary current method described by Amm and Viljanen (1999). Then this is used to derive a modeled ground magnetic field over a grid which equates to ~65 km at the region of interest. We then interpolate the magnetic field at the node locations from the modeled magnetic field values. This region is densely populated by IMAGE stations, so the accuracy of deriving the equivalent currents should be optimal over this area. In addition, this particular interval and location were chosen since it demonstrated significant intensifications of the ionospheric currents and subsequent spatiotemporal variations. It was also when the largest peak GIC was measured in the Finnish natural gas pipeline located in Mäntsälä, which was studied in detail by Dimmock et al. (2019). For the geomagnetic induction, we use the realistic 3-D ground conductivity model described in section 2.3.

Finally, each horizontal and vertical line segment of the grid indicated by the dashed blue and solid red lines are considered as transmission lines, in which we compute the voltage according to

$$V_{x,y} = \int_L E_{(x,y)} \cdot \hat{n} \mathrm{d}s, \tag{1}$$

where $E_{x,y}$ is the geoelectric field in either x or y directions, and $\hat{n}$ is the unit vector parallel to the line. This is a simplified case since the line (L) is either along the x or y direction and has no connections to other lines. Real power grids have several connected lines, many grounding points and a complex geometry. However, for the present purpose, studying single straight lines reveals more clearly the effect of nonuniform magnetic fields.

This procedure is repeated for two cases. The first case is when $B_{x,y}$ is known for each node, and therefore used to derive $E_{x,y}$. The second case is when $B_{x,y}$ is only known for one node along the line, and thus the same $B_{x,y}$ is used to calculate $E_{x,y}$ at each node, that is, a plane wave primary field is assumed. This second case is repeated for the number of nodes (21) in a given line. Therefore, in practice, for each line, method one gives one voltage time series, whereas method two yields a 21 time series equal to the number of nodes. The second case represents a real example when only a single magnetic recording might be available over the spatial extent of a line. In such a case, it is not possible to include the spatial variations of the magnetic field in the GIC modeling process. Any differences in voltages between the two cases are entirely driven by the spatial structure of the magnetic field.

The grid is then shifted by 100 km and this entire procedure is then repeated but for lines not covered by the previous grid. Therefore, some lines have a 50% overlap between one grid and the next but there are no completely repeated lines. Figure 8b shows the locations where this grid was placed; these were selected because the density of IMAGE observatories is the highest, and the previously presented statistics (Region 2) were also collected around this area. We see from Figure 8b that there is a 5×5 grid of red squares indicating the grid centers. Therefore, each row/column in this grid has 61 unique lines resulting in a total of 305 (61×5) horizontal and vertical lines of a length of 200 km. Along each line we compute a peak voltage, so in total there are 610 data points.

To compare results from both cases, the maximum absolute voltage is taken from each voltage time series (17:15–19:15 UT on 8 September 2017), and then the relative percent difference (*RPD*) is computed between the value from method one and the value from method two. The RPD is defined as

$$RPD = 100 \times \left(\frac{\max[|V_1|] - \max[|V_2|]}{\max[|V_1|]} \right), \quad (2)$$

where subscripts 1 and 2 correspond to methods one and two, respectively. Note that the V_1 and V_2 maxima do not necessarily occur at the same time, but the purpose is to compare the peak voltages measured during this interval. A histogram of the relative percentage difference is shown in Figure 9. Solid and dashed black lines indicate north-south and east-west lines, respectively (305 points each). The relative difference between maximum voltages from both north-south and east-west lines do not show any significant differences. In reality, this means that the spatiotemporal features of the ground magnetic field were not completely aligned in one direction even though the depressions are larger in the north-south direction. The bulk of the distribution is below 20%, meaning that for many cases, the spatial structure of the magnetic field has little effect on the maximum voltage. Having said that, there are significant amounts of data points between 20% and 40%, suggesting a moderate effect. More importantly, some data points reach almost 60%. This last point indicates that in some cases, even over 200 km, better resolution of the spatial geomagnetic structure results in significant differences in the peak voltage.

5. Discussion

This study aimed to quantify the extent of the spatial variations of the horizontal d*B*/d*t* (d*H*/d*t*) over regional (500 km) scales at high latitudes, investigate possible solar wind dependencies, and determine their significance to GICs. The motivation for this study has been the recent focus (e.g., Bedrosian & Love, 2015; Love et al., 2019; Ngwira et al., 2018, 2015; Pulkkinen et al., 2003; Viljanen & Pirjola, 2017) on advancing our understanding of the importance of regional effects on GICs. We have devised a method to statistically measure the regional variation of d*B*/d*t* by comparing spatial averages of d*H*/d*t* to individual station measurements, denoted as *RSD*. It was evident that d*H*/d*t* varies significantly over spatial scales even on the order of hundreds of kilometers and can surprisingly exceed the regional average by a factor of 3. As expected, our results indicate that this was strongly coupled to both the energy deposited into the magnetosphere and the derived geomagnetic auroral indices. A real example from the heavily studied (Dimmock et al., 2019) September 2017 period was used to demonstrate that accounting for spatial variations of geomagnetic structures can result in up to 60% differences in the peak voltage over a 200 km transmission line.

The large degree of variability of d*H*/d*t* was first demonstrated in Figure 4 by comparing *RSD* and the regional average. Geomagnetic activity can be considered as a period in which the geomagnetic field increases or decreases from its long-term average level, resulting from the enhancement of electrical ionospheric and magnetospheric currents flowing above. When these currents exhibit significant spatiotemporal variations, then the derivative of the geomagnetic field will also enhance accordingly, which can be used as a proxy to intervals that are prone to driving large GICs (Viljanen et al., 2015). What is important to note is that Figure 4 shows that even when d*H*/d*t* is high over a region, the individual stations within that region can measure significantly different individual values, sometimes by several times. This effect appears to be more noticeable during larger regional d*H*/d*t* since the behavior of the ionospheric currents becomes complex and highly structured. Small scale current structures embedded within larger-scale current systems can enhance d*H*/d*t* over a given region, and in some situations, vortex structures can develop, (e.g., Belakhovsky et al., 2019). Such structures will drive a spatially complex d*B*/d*t*. Besides, substorms can often be triggered during geomagnetic storms, producing large d*H*/d*t* and can be particularly localized (Ngwira et al., 2018). Therefore, we believe that, statistically, during stronger storms, these (known) magnetosphere-ionosphere coupling processes induce complex, rapid, and relatively localized behavior of the ionospheric currents that subsequently drive complex geomagnetic responses on the ground.

Substorm-related geomagnetic responses are likely highly spatially structured, meaning that characterizing a regional d*H*/d*t* with an individual station will introduce large errors, as indicated by Figure 4. Evidence of this is supported by Figure 5, which suggests that the *RSD* is coupled to the strength of auroral geomagnetic activity based on the locally derived IE index. Another way to look at this is that, in

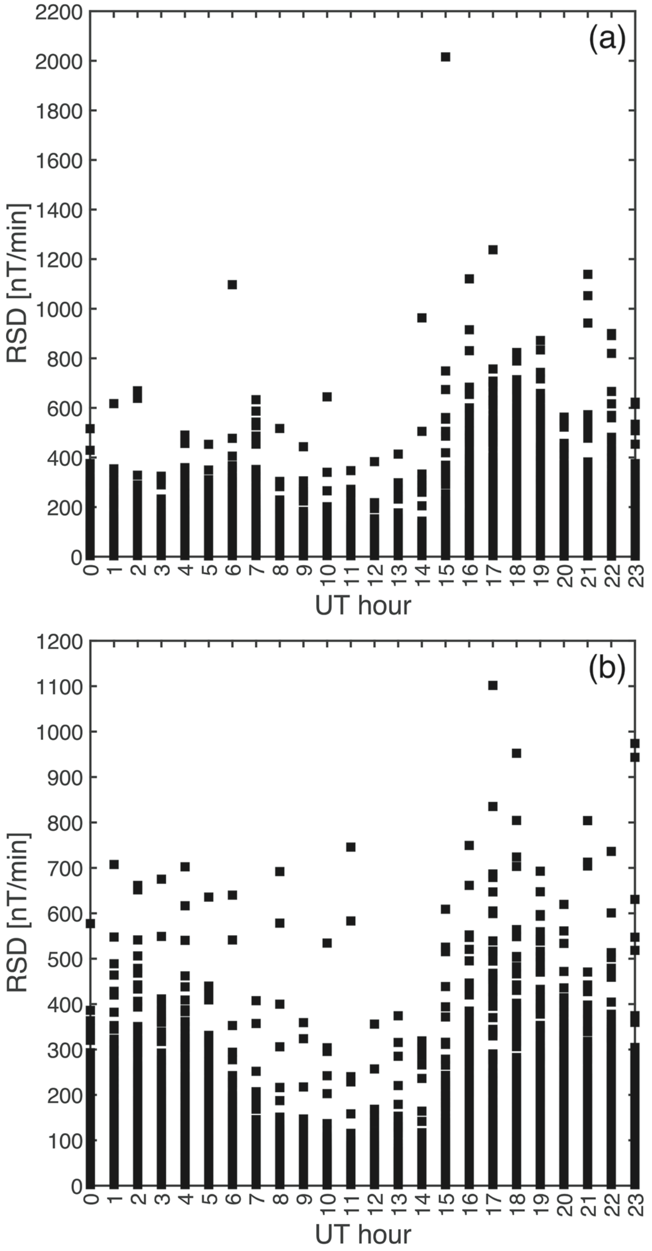

Figure 10. Scatter plot of *RSD* as a function of the UT hour in which the peak *RSD* was recorded. Panels (a(and (b) show data compiled separated for regions one and two. There is a clear diurnal trend where the largest *RSD* is around premidnight, which could be related to substorm activity. Although the lowest *RSD* is close to noon, larger values at these times may be due to impulsive events such as interplanetary shocks.

general, the dH/dt will increase with the amplitude of the magnetic field variation, but the spread for a given field variation is large. Although the IE index is useful to determine the lower range, it is not possible to predict a specific value. Nevertheless, geomagnetic indices do provide some useful insights into the activity level over a large region. However, the effectiveness of geomagnetic indices for other purposes has been debated for some time, particularly their ability to identify substorms (Kamide & Akasofu, 1983).

The use of regional averages was suggested by Pulkkinen et al. (2015) and may provide improvements over using a single station since some regional variability is taken into account. Our study agrees with this assessment and also that predicting dB/dt over a geographic region rather than at a specific station may be more feasible and provide higher skill. This is in line with Pulkkinen, Klimas, et al. (2006), who performed a spatiotemporal structure function analysis of IMAGE data. They found that the behavior of dB/dt above temporal scales of hundreds resembles that of uncorrelated white noise. This sets unavoidable constraints on the forecasting accuracy of dB/dt. Additionally, they showed that spatial symmetry of the horizontal magnetic field fluctuations increases during substorms. In other words, ionospheric currents then have a more complex spatial structure.

During southward IMF, reconnection is initiated on the dayside magnetopause which transfers magnetic flux to the tail and increases convection within the magnetosphere. During this time, substorms can be triggered (Akasofu, 1964; Kan et al., 1991) by either internal (magnetotail) or external (solar wind) physical processes. Importantly, substorms have been reported as a mechanism capable of driving localized geoelectric fields (Clilverd et al., 2018; Ngwira et al., 2015, 2018; Pulkkinen et al., 2003, 2015; Viljanen, Tanskanen, et al. 2006). If substorms are of such importance, then there would be an expected diurnal trend in *RSD* favored around midnight due to the closure of the substorm current wedge field-aligned current (Akasofu, 1964). To check this, we plot the *RSD* as a function of the local hour in UT in Figure 10 for both subset regions. There is a clear diurnal trend in both regions such that the largest *RSD* tends to occur around the premidnight sector. This trend is consistent with substorm activity and is supported by Viljanen, Tanskanen, et al. (2006), who reported that the largest dB/dt in this region tends to occur due to substorms around midnight.

Previous statistical studies such as Weigel et al. (2003) and Juusola et al. (2015) concerning dB/dt, or the time derivative of ionospheric equivalent current densities, provide a general background to understand how the solar wind affects geomagnetic variations at high latitudes. It is interesting to note that according to Weigel et al. (2003), the process that drives variations of the ground northward field (B_x) is different from that which drives dB_x/dt. This could be understood in terms of spatially rather smooth electrojets of large amplitudes that give the largest contribution to B_x, whereas rapidly varying small-scale currents give an additional significant contribution to dB_x/dt. As both Weigel et al. (2003) and Juusola et al. (2015) demonstrate, there is no single solar wind parameter that could explain the observed features, but there is a clear dependence of the location and local time.

Further evidence is provided by Figure 6, in which the largest *RSD* is occurring during strongly southward IMF, a condition associated with substorm activity. Figure 7demonstrated this even clearer, suggesting that the solar wind convective electric field, often used as a proxy for the dayside reconnection rate, is also a key upstream parameter. Nevertheless, our results strongly indicate that regional variability at these latitudes is inherently linked to the amount of energy that is deposited into the magnetosphere, which increases the likelihood of substorms and advanced convection. Finally, we should note that even during northward IMF, some significant regional variability was noticeable during faster solar wind speeds. Studies have shown that impulsive events such as interplanetary shocks may have the capacity to be important to GICs (Kappenman, 2003), which are likely present in our statistical data. It should also be mentioned that the recent work by Nykyri et al. (2019) has demonstrated that substorms can even be triggered during northward IMF by dayside transients, a high-speed jet (Hietala et al., 2012) in their case. In agreement with these studies suggesting that high geomagnetic activity can occur during unexpected conditions, it is clear that further work is required to determine the importance and frequency of these events.

Our results indicate that these results are important to GICs in some situations, as presented in Figure 9. It is shown that spatial-scale geomagnetic variations on the order of hundreds of kilometers can result in up to a 60% difference in GICs across a transmission line of 200-km length. Viljanen and Pirjola (2017) explicitly investigated the effects on similar scales, but from variations in the geoelectric field vector direction instead of magnitude; even so, their results converge on a similar conclusion to ours. That is, accurate modeling of GICs requires that the spatial structure of the geomagnetic variations should be taken into account with the scale of the network. This work was also only performed for one interval, and therefore these effects may be larger for other stronger storms and different latitudes where the behavior of the ionospheric currents is more dynamic.

It seems that in Figures 4 and 5, there are differences between the two regions in terms of regional variability. In general, the polar cap magnetometers recorded a high level of *RSD* even for very low spatial averages. This indicates that the nature of the ionospheric currents at these latitude ranges is different. Region one stations will typically experience a higher degree of geomagnetic activity compared to region two and will capture the initial substorm expansion phase before the auroral oval moves equatorward (Milan et al., 2017). It has been reported that the amplitude of $\mathrm{d}B/\mathrm{d}t$ increases with latitude (Engebretson et al., 2019), suggesting the spatiotemporal variations of currents at poleward currents are increased. Thus, at latitudes around 70°, the regional variability appears less ordered, and correlating this with other parameters becomes more challenging. Nevertheless, the significance of GIC over region one is low due to the lack of large population centers; however, this does demonstrate the need to investigate the localized nature of ionospheric currents at different latitudes. When additional magnetometers are added to IMAGE at southern latitudes, this work should be repeated to investigate the regions of Fennoscandia which contain large populations such as southern Sweden, especially since this region is prone to high geoelectric fields (Rosenqvist & Hall, 2019).

We remind readers that the magnetic field variation measured on the ground is primarily produced by currents in space and secondarily by induced (telluric) currents in the Earth. In the region under study, the internal contribution to the horizontal field can be up to a few tens of percent (Tanskanen et al., 2001). As shown by Viljanen et al. (2001), the orientation of $\mathrm{d}H/\mathrm{d}t$ is much more scattered than that of the corresponding H vector (at least for time steps when $\mathrm{d}H/\mathrm{d}t>1$ nT/s). There are two reasons for this. First, the orientation of H is typically dominated by large-scale and strong eastward or westward electrojets, whereas $\mathrm{d}H/\mathrm{d}t$ is affected also by small-scale currents without a preferred flow direction. Second, ground conductivity anomalies must be taken into account. A clear example shown by Viljanen et al. (2001) is the LYC station (not used in this paper), where $\mathrm{d}H/\mathrm{d}t$ vectors tend to orientate strongly to the (geographic) NNE-SSW direction and are clearly different from the preferred NNW-SSE direction of H. Although the main driver of geomagnetic variations is currents in the ionosphere and magnetosphere, the effect of telluric currents must also be considered, and they are specific for each region. An example of the importance of large conductivity gradients in Fennoscandia is the well-known coastal effect caused by the transition between a conductive ocean and resistive ground (Rosenqvist & Hall, 2019). Similar gradients also occur inland, causing complex geoelectric field enhancements and polarizations, depending on the spatial and temporal features of the primary ionospheric-magnetospheric magnetic field.

Finally, to check the role of telluric currents on $\mathrm{d}H/\mathrm{d}t$, we have plotted in Figure 11 a histogram of the region two stations where the 30-min maximum *RSD* originated. It is clear that the MAS station contributes significantly to the RSD statistics. According to Figure 2, there are some conductivity anomalies in that region.

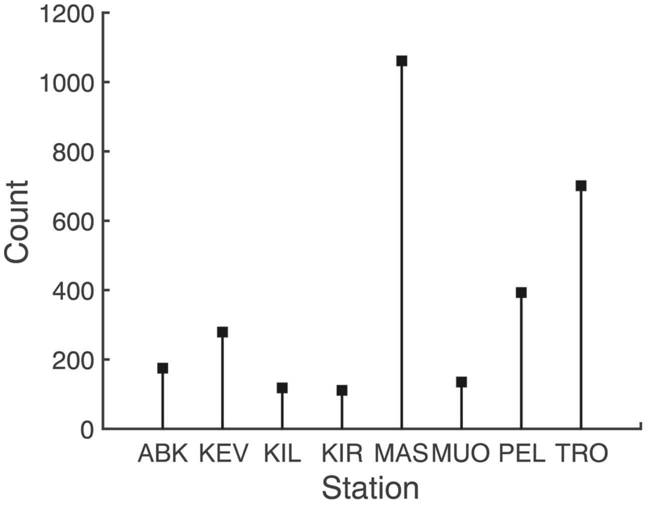

Figure 11. Histogram showing the stations which were responsible for the largest *RSD*. Note that the MAS station appears to be statistically significant.

The motivation for this paper was to investigate the regional variability of d*B*/d*t* measured from magnetometers, and according to Figure 11 one cannot always ignore the internal contribution to d*B*/d*t*, although the role it plays on the geomagnetic depression is likely small. Viljanen et al. (2001) showed this to be the case for the LYC station, and thus future studies that analyze d*B*/d*t* should have adequate knowledge of the local ground conductivity. This reiterates the picture formed by these results, that one station is sometimes inadequate to characterize d*B*/d*t* over even a localized region. This is also particularly important in the field of space weather machine learning if models are to be trained using single stations. Separating internal and external components is not trivial and not the focus of this study; however, efforts are ongoing to implement this with the IMAGE data, meaning this effect can be studied in greater detail to better understand the true role of telluric currents on d*B*/d*t*.

5.1. Future Implications

The present study highlights the complex fine spatial and temporal structures of the geomagnetic field time derivative and the need to understand its behavior on regional scales. There are several implications of relevance to point out. First, it will be important to characterize the extent of spatial variations of the geomagnetic field at different latitudes since it may be of interest in assessing error on d*B*/d*t* predictions. This is also important since we noticed discrepancies in statistical behavior between two subsets located at different latitudes. Second, as the understanding of more localized effects improves, it is becoming clear that denser and comprehensive magnetic observatories are needed to resolve such features. Third, it appears that a high degree of regional variability is not so uncommon in strong storms ($AE > 300$ nT), and the sources of this may be varied and unspecific. On the other hand, strong evidence persists that substorms are important (Ngwira et al., 2018; Tsurutani et al., 2015), and future research to clarify their role is required. Finally, for accurate modeling of GICs, especially during strong storms, at least two or more magnetic measurements must be employed to characterize the geomagnetic field over regions on the order of hundreds of kilometers. Of course, the work presented here represents a simplified case of straight and independent transmission lines, and it will be important to perform similar analysis on realistic power grids. This work should be carried out with the continued investment in magnetotelluric surveys, considering that the local geology plays a large role in localized geoelectric field features (Bedrosian & Love, 2015) and can also significantly affect d*B*/d*t*. This last point suggests that when utilizing d*B*/d*t* as a regional GIC proxy, the user should be aware of any local geological anomalies which can create sharp gradients in conductivity. Finally, it is important to consider these results in context with d*B*/d*t* predictions from global MHD models, which was recently discussed by Welling (2019) based on recent and ongoing efforts (e.g., Honkonen et al., 2018; Tóth et al., 2014). Although our results suggest that regional variations are important to the GIC modeling process, the capability of global MHD models to resolve spatially structured geomagnetic disturbances is unclear. It will be crucial moving forward to assess the performance of these simulations with respect to localized disturbances.

6. Summary and Conclusions

The analysis performed in the present study has led to many new insights into the regional variability of d*B*/d*t* and its possible impact on GICs. These are listed below:

1. Over regional 500-km spatial scales, the horizontal magnetic field derivative typically varies as much as the spatial average, and in some cases by several times that.
2. Locally derived geomagnetic indices provide a more accurate statistical relationship to the regional variability, but the range of regional variability remains large. Having said that, the applicability of auroral indices (e.g., AL, AU, AE) to predict upper and lower limits of d*B*/d*t* seems promising.
3. Enhanced regional variability is linked to increased energy deposition into the magnetosphere during southward IMF and faster solar wind speeds. On the other hand, other events such as interplanetary shocks may be able to produce similar effects during northward IMF.

4. Even over a 200-km transmission line, spatial variations of the geomagnetic field can result in up to 60% difference in peak voltages compared to when a uniform magnetic field is assumed.
5. From a statistical standpoint, a clear diurnal trend was present, suggesting that substorms may be important to explaining regional variations at the latitudes considered. This will remain a fundamental line of research to better understand localized geomagnetic phenomena.
6. In the application of dB/dt as a GIC proxy, the local ground conductivity can influence dB/dt as has been demonstrated over some regions of Fennoscandia covered by the IMAGE network. Future studies should be aware of local conductivity anomalies that can affect the derived dB/dt from individual stations.

To summarize, recent studies have shown the importance of understanding regional variability of the geomagnetic field and its time derivative. This work makes a significant contribution to this effort by quantifying the variation, highlighting key upstream dependencies, and evaluating its impact on GICs. There are still many unanswered questions to address, such as the following: (1) How does this change across different latitudes? (2) Can a regional variability benchmark for extreme events be determined? (3) What are the responsible magnetosphere-ionosphere physical coupling mechanisms? (4) Is MHD capable of handling regional effects? The most important question, however, is (5) whether these works can be applied in operational space weather to improve regional forecasts. Although more work is needed, it is clear that significant advances are being made, and the picture in terms of technical and physical requirements is becoming clearer, which should translate to operations at some stage in the future.

Appendix A: Bin Densities for Figure 7d

Figure A1 is a reproduction of Figure 7d, but the color shows the number of points per bin on a log scale.

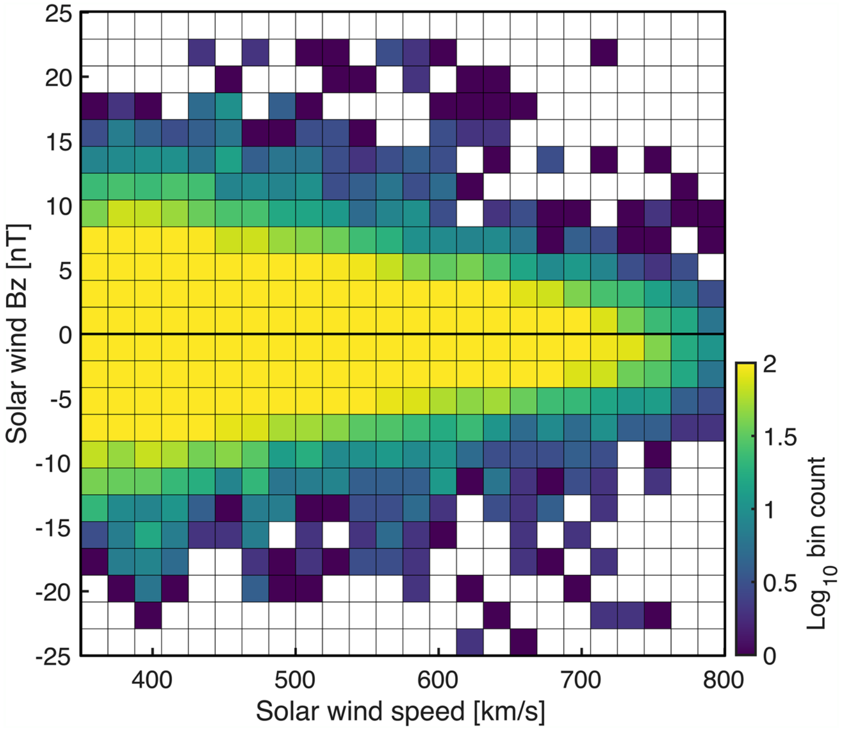

Figure A1. Same as figure 6d but the color represents the number of points per bin.

Data Availability Statement

The IMAGE data and its derived data products can be obtained free of charge at this site (http://space.fmi.fi/image). OMNI data are available via the NASA OMNIWeb service at https://omniweb.gsfc.nasa.gov/, which includes solar wind parameters and geomagnetic indices. The SMAP model conductivity profiles of Fennoscandia and their derivation can be found in the following manuscripts (Engels & Korja, 2002; Korja et al., 2002).

Acknowledgments

A. P. D., E. Y., and L. R. were funded by the Swedish Civil Contingencies Agency Grant 2016-2102. The work by I. H. and A. V. was supported by the Academy of Finland Grant 314670. R. J. B. has received financial support from the UK NERC under Grant NE/P017061/1. D. W. was supported by the National Science Foundation Award ICER-1663770. We thank the institutes that maintain the IMAGE Magnetometer Array: Tromsø Geophysical Observatory of UiT the Arctic University of Norway (Norway), Finnish Meteorological Institute (Finland), Institute of Geophysics Polish Academy of Sciences (Poland), GFZ German Research Centre for Geosciences (Germany), Geological Survey of Sweden (Sweden), Swedish Institute of Space Physics (Sweden), Sodankylä Geophysical Observatory of the University of Oulu (Finland), and Polar Geophysical Institute (Russia). Thank you to Liisa Juusola (FMI, Finland) for discussion and comments on the manuscript.

References

Akasofu, S. I. (1964). The development of the auroral substorm. *Planetary and Space Science*, *12*(4), 273–282. https://doi.org/10.1016/0032-0633(64)90151-5

Amm, O., & Viljanen, A. (1999). Ionospheric disturbance magnetic field continuation from the ground to the ionosphere using spherical elementary current systems. *Earth, Planets and Space*, *51*(6), 431–440. https://doi.org/10.1186/BF03352247

Anderson, C. W., Lanzerotti, L. J., & MacLennan, C. G. (1974). Outage of the L4 system and the geomagnetic disturbances of 4 August 1972. *Bell System Technical Journal*, *53*(9), 1817–1837. https://doi.org/10.1002/j.1538-7305.1974.tb02817.x

Apatenkov, S. V., Pilipenko, V. A., Gordeev, E. I., Viljanen, A., Juusola, L., Belakhovsky, V. B., & Selivanov, V. N. (2020). Auroral omega bands are a significant cause of large geomagnetically induced currents. *Geophysical Research Letters*, *47*, e2019GL086677. https://doi.org/10.1029/2019GL086677

Bedrosian, P. A., & Love, J. J. (2015). Mapping geoelectric fields during magnetic storms: Synthetic analysis of empirical United States impedances. *Geophysical Research Letters*, *42*, 10,160–10,170. https://doi.org/10.1002/2015GL066636

Belakhovsky, V., Pilipenko, V., Engebretson, M., Sakharov, Y., & Selivanov, Y. (2019). Impulsive disturbances of the geomagnetic field as a cause of induced currents of electric power lines. *Journal of Space Weather and Space Climate*, *9*, A18. https://doi.org/10.1051/swsc/2019015

Bolduc, L. (2002). GIC observations and studies in the Hydro-Québec power system. *Journal of Atmospheric and Solar-Terrestrial Physics*, *64*(16), 1793–1802. https://doi.org/10.1016/S1364-6826(02)00128-1

Boteler, D. H., & Jansen Van Beek, G. (1999). August 4, 1972 revisited: A new look at the geomagnetic disturbance that caused the L4 cable system outage. *Geophysical Research Letters*, *26*(5), 577–580. https://doi.org/10.1029/1999GL900035

Clilverd, M. A., Rodger, C. J., Brundell, J. B., Dalzell, M., Martin, I., Mac Manus, D. H., & Obana, Y. (2018). Long-lasting geomagnetically induced currents and harmonic distortion observed in New Zealand during the 7–8 September 2017 disturbed period. *Space Weather*, *16*, 704–717. https://doi.org/10.1029/2018SW001822

Dimmock, A., Rosenqvist, L., Hall, J., Viljanen, A., Yordanova, E., Honkonen, I., & Sjöberg, E. (2019). The GIC and geomagnetic response over Fennoscandia to the 7–8 September 2017 geomagnetic storm. *Space Weather*, *17*, 989–1010. https://doi.org/10.1029/2018SW002132

Eastwood, J. P., Biffis, E., Hapgood, M. A., Green, L., Bisi, M. M., Bentley, R. D., & Burnett, C. (2017). The economic impact of space weather: Where do we stand? *Risk Analysis*, *37*(2), 206–218. https://doi.org/10.1111/risa.12765

Engebretson, M. J., Pilipenko, V. A., Ahmed, L. Y., Posch, J. L., Steinmetz, E. S., Moldwin, M. B., & Vorobev, A. V. (2019). Nighttime magnetic perturbation events observed in Arctic Canada: 1. Survey and statistical analysis. *Journal of Geophysical Research: Space Physics*, *124*, 7442–7458. https://doi.org/10.1029/2019JA026794

Engels, M., & Korja, T. (2002). Multisheet modelling of the electrical conductivity structure in the Fennoscandian Shield. *Earth, Planets and Space*, *54*(5), 559–573. https://doi.org/10.1186/BF03353045

Farris, M. H., & Russell, C. T. (1994). Determining the standoff distance of the bow shock: Mach number dependence and use of models. *Journal of Geophysical Research*, *99*(A9), 17,681. https://doi.org/10.1029/94ja01020

Freeman, M. P., Forsyth, C., & Rae, I. J. (2019). The influence of substorms on extreme rates of change of the surface horizontal magnetic field in the United Kingdom. *Space Weather*, *17*, 827–844. https://doi.org/10.1029/2018SW002148

Hietala, H., Partamies, N., Laitinen, T. V., Clausen, L. B., Facskò, G., Vaivads, A., & Lucek, E. A. (2012). Supermagnetosonic subsolar magnetosheath jets and their effects: From the solar wind to the ionospheric convection. *Annales Geophysicae*, *30*(1), 33–48. https://doi.org/10.5194/angeo-30-33-2012

Honkonen, I., Kuvshinov, A., Rastätter, L., & Pulkkinen, A. (2018). Predicting global ground geoelectric field with coupled geospace and three-dimensional geomagnetic induction models. *Space Weather*, *16*, 1028–1041. https://doi.org/10.1029/2018SW001859

Ivannikova, E., Kruglyakov, M., Kuvshinov, A., Rastätter, L., & Pulkkinen, A. A. (2018). Regional 3-D modeling of ground electromagnetic field due to realistic geomagnetic disturbances. *Space Weather*, *16*, 476–500. https://doi.org/10.1002/2017SW001793

Juusola, L., Kauristie, K., van de Kamp, M., Tanskanen, E. I., Mursula, K., Asikainen, T., & Viljanen, A. (2015). Solar wind control of ionospheric equivalent currents and their time derivatives. *Journal of Geophysical Research: Space Physics*, *120*, 4971–4992. https://doi.org/10.1002/2015JA021204

Kamide, Y., & Akasofu, S. I. (1983). Notes on the auroral electrojet indices. *Reviews of Geophysics*, *21*(7), 1647–1656. https://doi.org/10.1029/RG021i007p01647

Kan, J. R., Potemra, T. A., Kokubun, S., & Iijima, T. (1991). Magnetospheric substorms. Washington DC American Geophysical Union Geophysical Monograph Series, 64, https://doi.org/10.1029/GM064

Kappenman, J. G. (2003). Storm sudden commencement events and the associated geomagnetically induced current risks to ground-based systems at low-latitude and midlatitude locations. *Space Weather*, *1*(3), 1016. https://doi.org/10.1029/2003sw000009

Kauristie, K., Pulkkinen, T. I., Pellinen, R. J., & Opgenoorth, H. J. (1996). What can we tell about global auroral-electrojet activity from a single meridional magnetometer data? *Annales Geophysicae*, *14*, 1177–1185. https://doi.org/10.1007/s00585-996-1177-1

Kelbert, A. (2020). The role of global/regional Earth conductivity models in natural geomagnetic hazard mitigation. *Surveys in Geophysics*, *41*(115), 115–166. https://doi.org/10.1007/s10712-019-09579-z

King, J. H., & Papitashvili, N. E. (2005). Solar wind spatial scales in and comparisons of hourly Wind and ACE plasma and magnetic field data. *Journal of Geophysical Research*, *110*, A02104. https://doi.org/10.1029/2004JA010649

Korja, T., Engels, M., Zhamaletdinov, A. A., Kovtun, A. A., Palshin, N. A., Smirnov, M. Y., & Vardaniants, I. L. (2002). Crustal conductivity in Fennoscandia—A compilation of a database on crustal conductance in the Fennoscandian Shield. *Earth, Planets and Space*, *54*(5), 535–558. https://doi.org/10.1186/BF03353044

Lehtinen, M., & Pirjola, R. (1985). Currents produced in earthed conductor networks by geomagnetically-induced electric fields. *Annales Geophysicae*, *3*(4), 479.

Liu, C., Wang, X., Wang, H., & Zhao, H. (2018). Quantitative influence of coast effect on geomagnetically induced currents in power grids: A case study. *Journal of Space Weather and Space Climate*, *8*, A60. https://doi.org/10.1051/swsc/2018046

Love, J. J., Lucas, G. M., Bedrosian, P. A., & Kelbert, A. (2019). Extreme-value geoelectric amplitude and polarization across the Northeast United States. *Space Weather*, *17*, 379–395. https://doi.org/10.1029/2018SW002068

Milan, S. E., Clausen, L. B., Coxon, J. C., Carter, J. A., Walach, M. T., Laundal, K., & Anderson, B. J. (2017). Overview of solar wind-magnetosphere-ionosphere-atmosphere coupling and the generation of magnetospheric currents. *Space Science Reviews*, *206*(1-4), 547–573. https://doi.org/10.1007/s11214-017-0333-0

Ngwira, C. M., Pulkkinen, A. A., Bernabeu, E., Eichner, J., Viljanen, A., & Crowley, G. (2015). Characteristics of extreme geoelectric fields and their possible causes: Localized peak enhancements. *Geophysical Research Letters*, *42*, 6916–6921. https://doi.org/10.1002/2015GL065061

Ngwira, C. M., Sibeck, D., Silveira, M. V. D., Georgiou, M., Weygand, J. M., Nishimura, Y., & Hampton, D. (2018). A study of intense local dB/dt variations during two geomagnetic storms. *Space Weather*, *16*, 676–693. https://doi.org/10.1029/2018sw001911

Nykyri, K., Bengtson, M., Angelopoulos, V., Nishimura, Y., & Wing, S. (2019). Can enhanced flux loading by high-speed jets lead to a substorm? Multipoint detection of the christmas Day substorm onset at 08:17 UT, 2015. *Journal of Geophysical Research: Space Physics*, *124*, 4314–4340. https://doi.org/10.1029/2018JA026357

Pulkkinen, A. (2015). Geomagnetically induced currents modeling and forecasting. *Space Weather*, *13*, 734–736. https://doi.org/10.1002/2015SW001316

Pulkkinen, A., Bernabeu, E., Eichner, J., Viljanen, A., & Ngwira, C. (2015). Regional-scale high-latitude extreme geoelectric fields pertaining to geomagnetically induced currents. *Earth, Planets and Space*, *67*(1), 93. https://doi.org/10.1186/s40623-015-0255-6

Pulkkinen, A., Bernabeu, E., Thomson, A., Viljanen, A., Pirjola, R., Boteler, D., & MacAlester, M. (2017). Geomagnetically induced currents: Science, engineering, and applications readiness. *Space Weather*, *15*, 828–856. https://doi.org/10.1002/2016SW001501

Pulkkinen, A., Klimas, A., Vassiliadis, D., Uritsky, V., & Tanskanen, E. (2006). Spatiotemporal scaling properties of the ground geomagnetic field variations. *Journal of Geophysical Research*, *111*, A03305. https://doi.org/10.1029/2005JA011294

Pulkkinen, A., Lindahl, S., Viljanen, A., & Pirjola, R. (2005). Geomagnetic storm of 29–31 October 2003: Geomagnetically induced currents and their relation to problems in the Swedish high-voltage power transmission system. *Space Weather*, *3*, S08C03. https://doi.org/10.1029/2004SW000123

Pulkkinen, A., Rastätter, L., Kuznetsova, M., Singer, H., Balch, C., Weimer, D., & Weigel, R. (2013). Community-wide validation of geospace model ground magnetic field perturbation predictions to support model transition to operations. *Space Weather*, *11*, 369–385. https://doi.org/10.1002/swe.20056

Pulkkinen, A., Thomson, A., Clarke, E., & McKay, A. (2003). April 2000 geomagnetic storm: Ionospheric drivers of large geomagnetically induced currents. *Annales Geophysicae*, *21*(3), 709–717. https://doi.org/10.5194/angeo-21-709-2003

Pulkkinen, A., Viljanen, A., & Pirjola, R. (2006). Estimation of geomagnetically induced current levels from different input data. *Space Weather*, *4*, S08005. https://doi.org/10.1029/2006SW000229

Rosenqvist, L., & Hall, J. O. (2019). Regional 3-D modeling and verification of geomagnetically induced currents in Sweden. *Space Weather*, *17*, 27–36. https://doi.org/10.1029/2018SW002084

Rosenqvist, L., Opgenoorth, H., Buchert, S., McCrea, I., Amm, O., & Lathuillere, C. (2005). Extreme solar-terrestrial events of October 2003: High-latitude and Cluster observations of the large geomagnetic disturbances on 30 October. *Journal of Geophysical Research*, *110*, A09S23. https://doi.org/10.1029/2004JA010927

Tóth, G., Meng, X., Gombosi, T. I., & Rastätter, L. (2014). Predicting the time derivative of local magnetic perturbations. *Journal of Geophysical Research: Space Physics*, *119*, 310–321. https://doi.org/10.1002/2013JA019456

Tóth, G., Sokolov, I. V., Gombosi, T. I., Chesney, D. R., Clauer, C. R., De Zeeuw, D. L., & Kóta, J. (2005). Space weather modeling framework: A new tool for the space science community. *Journal of Geophysical Research*, *110*, A12226. https://doi.org/10.1029/2005JA011126

Tanskanen, E. I. (2009). A comprehensive high-throughput analysis of substorms observed by IMAGE magnetometer network: Years 1993–2003 examined. *Journal of Geophysical Research*, *114*, A05204. https://doi.org/10.1029/2008JA013682

Tanskanen, E. I., Viljanen, A., Pulkkinen, Pirjola, Häkkinen, L., Pulkkinen, A., & Amm, O. (2001). At substorm onset, 40% of AL comes from underground. *Journal of Geophysical Research*, *106*, 13,119–13,134. https://doi.org/10.1029/2000JA900135

Tsurutani, B. T., Hajra, R., Echer, E., & Gjerloev, J. W. (2015). Extremely intense (SML *le* 2500 nT) substorms: Isolated events that are externally triggered? *Annales Geophysicae*, *33*(5), 519–524. https://doi.org/10.5194/angeo-33-519-2015

Viljanen, A. (1997). The relation between geomagnetic variations and their time derivatives and implications for estimation of induction risks. *Geophysical Research Letters*, *24*(6), 631–634. https://doi.org/10.1029/97GL00538

Viljanen, A., Nevanlinna, H., Pajunpää, K., & Pulkkinen, A. (2001). Time derivative of the horizontal geomagnetic field as an activity indicator. *Annales Geophysicae*, *19*(9), 1107–1118. https://doi.org/10.5194/angeo-19-1107-2001

Viljanen, A., & Pirjola, R. (2017). Influence of spatial variations of the geoelectric field on geomagnetically induced currents. *Journal of Space Weather and Space Climate*, *7*, A22. https://doi.org/10.1051/swsc/2017024

Viljanen, A., Pulkkinen, A., Pirjola, R., Pajunpää, K., Posio, P., & Koistinen, A. (2006). Recordings of geomagnetically induced currents and a nowcasting service of the Finnish natural gas pipeline system. *Space Weather*, *4*, S10004. https://doi.org/10.1029/2006SW000234

Viljanen, A., Tanskanen, E. I., & Pulkkinen, A. (2006). Relation between substorm characteristics and rapid temporal variations of the ground magnetic field. *Annales Geophysicae*, *24*(2), 725–733. https://doi.org/10.5194/angeo-24-725-2006

Viljanen, A., Wintoft, P., & Wik, M. (2015). Regional estimation of geomagnetically induced currents based on the local magnetic or electric field. *Journal of Space Weather and Space Climate*, *5*, A24. https://doi.org/10.1051/swsc/2015022

Weigel, R. S., Klimas, A. J., & Vassiliadis, D. (2003). Solar wind coupling to and predictability of ground magnetic fields and their time derivatives. *Journal of Geophysical Research*, *108*(A7), 1298. https://doi.org/10.1029/2002JA009627

Welling, D. (2019). Magnetohydrodynamic models of B and their use in GIC estimates. *Geomagnetically induced currents from the Sun to the power grid* (pp. 43–65). Washington, DC: American Geophysical Union (AGU). https://doi.org/10.1002/9781119434412.ch3